



Pulse-shaping method for real-time neutron/gamma discrimination at low sampling rates

Jia-Xin Li^{1,2} · Hui-Liang Hou^{1,2} · Yue-Feng Huang^{1,2} · Mao-Song Cheng^{1,2} · Zhi-Min Dai^{1,2}

Received: 29 March 2023 / Revised: 10 June 2023 / Accepted: 4 July 2023 / Published online: 14 November 2023

© The Author(s), under exclusive licence to China Science Publishing & Media Ltd. (Science Press), Shanghai Institute of Applied Physics, the Chinese Academy of Sciences, Chinese Nuclear Society 2023

Abstract

The NaI:Tl scintillator is an innovative material for dual-gamma-ray and neutron detection with a low ${}^6\text{Li}$ concentration. To achieve real-time n/γ discrimination, a zero-crossing time comparison algorithm based on trapezoidal pulse shaping was developed. The algorithm can operate efficiently at low sampling rates and was implemented on a single-probe portable digital n/γ discriminator based on a field-programmable gate array. The discriminator and NaI:Tl, ${}^6\text{Li}$ detector were tested in a neutron-gamma mixed field produced by an ${}^{241}\text{Am}$ -Be neutron source to evaluate the performance of the algorithm. The figure of merits was measured as 2.88 at a sampling rate of 50 MHz, indicating that the discriminator with its embedded algorithm has a promising n/γ discrimination capability. Efficient discrimination at sampling rates of 40 and 25 MHz demonstrates that the capability of this method is not limited by low sampling rates.

Keywords FPGA · NaI:Tl · ${}^6\text{Li}$ · Real time · Neutron/gamma discrimination · Pulse shaping

1 Introduction

Efficient neutron detection is in high demand in numerous fields, such as radiation monitoring [1], neutron imaging [2], and national security [3]. ${}^3\text{He}$ gaseous detectors are widely used in neutron detection systems. Although ${}^3\text{He}$ position-sensitive detectors show excellent neutron-gamma discrimination ability, reasonable spatial resolution (1–10 mm), and high count-rate capability [4], the high cost and shortage of ${}^3\text{He}$ limit their application. The world supply of ${}^3\text{He}$ used to come entirely from the decay of tritium originating from nuclear weapons programs in the USA and Russia [5]. The mainstream choice of neutron detectors has shifted to

scintillator detectors, including organic and inorganic scintillators. Because neutron emission is often accompanied by gamma rays, n/γ discrimination is a critical technique for neutron detection.

Scintillator detectors not only provide a high light yield and excellent energy resolution but also emit discriminative neutron pulse signals that can be extracted by pulse shape discrimination (PSD) methods [6]. Most PSD methods have been tested with plastic scintillators, such as EJ-276 and EJ-309, and most tested FoMs are better than 1.0 [7–10], which means that they can extract most neutron signals from mixed neutron-gamma radiation field. Plastic scintillators are preferred over liquid scintillators because of their attractive features, including low cost, self-containment, and ease of processing [10]. Among the anthracene, stilbene, and p-terphenyl scintillators, anthracene scintillators exhibit the highest light yield and PSD performance [11]. Inorganic scintillators have been developed using ${}^6\text{Li}(n, \alpha){}^3\text{H}$ reaction. The reasonable discrimination performance of elpasolite scintillators, such as CLYC, has been verified [12, 13]. As the latest inorganic scintillator, NaI:Tl, ${}^6\text{Li}$ is capable of efficient dual detection of thermal neutrons and gamma rays by doping with ${}^6\text{Li}$ while maintaining the original NaI:Tl scintillation properties. Moreover, NaI:Tl, ${}^6\text{Li}$ scintillators can be significantly larger than CLYCs [6].

This work was supported by the National Natural Science Foundation of China (NSFC) (No. 12075308).

✉ Hui-Liang Hou
houhuiliang@sinap.ac.cn

✉ Zhi-Min Dai
daizhimin@sinap.ac.cn

¹ Shanghai Institute of Applied Physics, Chinese Academy of Sciences, Shanghai 201800, China

² University of Chinese Academy of Sciences, Beijing 100049, China

In recent years, many time- and frequency-domain methods have been proposed and compared based on different features of the output signals from scintillators [7]. For example, the charge-comparison method integrates pulse signals and calculates the charge ratio in the time domain [7], whereas the discrete wavelet transform method calculates a scaling function that represents the energy density in the frequency domain [14]. Additionally, intelligent techniques such as neural networks have been applied to PSD [9, 15]. However, many matrix operations may be required in the frequency domain and artificial intelligence methods, which are limited to offline computing [15]. Such tedious and complex algorithms require long identification times; thus, they are not superior to fast real-time analysis. A confusing problem with time-domain methods is that their PSD performance is not as satisfactory as that of intelligence methods. One approach to solving this problem involves the use of pulse shaping, which can be applied to alter the features of the output signals from scintillators. A larger difference in signal shapes leads to better PSD performance. The pulse-shaping technique can decompose and synthesize signals in real time in an FPGA [16, 17] and potentially simplify PSD methods while maintaining good PSD performance.

Several digitizer boards are used to sample signals in most traditional PSD methods; however, a host computer is required for data processing [18–20]. A possible constraint for developing a real-time discriminator without a computer is the adaptability of the PSD algorithms. Additionally, to achieve better PSD performance, some algorithms have high hardware requirements [19–24], such as high sampling rates and large FPGA logic resources. However, the device size, power consumption, and cost have also been considered in some applications [25]. This paper proposes a time-domain algorithm based on a trapezoidal shaper to achieve real-time n/γ discrimination and demonstrates the feasibility of deploying this algorithm in a portable FPGA-based discriminator. The PSD performance was evaluated using a NaI:Tl,⁶Li scintillator at low sampling rates.

2 Method

2.1 Hardware design

A block schematic of the n/γ discriminator is shown in Fig. 1a. The n/γ discriminator receives signals from the NaI:Tl,⁶Li detector and uploads the latest spectra to a computer every 2 s. Most signal processing is performed in FPGA so the analog circuit only needs to satisfy the signal amplification and noise reduction requirements. After the neutron and gamma pulse signals are produced by the pre-amplifier, they must be further amplified and adjusted in the analog circuits of the discriminator. AD829 achieves its

230 V/ μ s uncompensated slew rate and 750 MHz gain bandwidth while requiring only 5 mA of current from power supplies, which is suitable for building a main amplifier. With a low input voltage noise of 1.7 nV/ $\sqrt{\text{Hz}}$, AD829 serves as an input buffer for an analog-to-digital converter (ADC). The amplified analog signals are then digitalized in a high-speed ADC (AD9236, Analog Device), which uses a multistage differential pipelined architecture to provide 12-bit resolution at up to 80 Msps. AD9236 operates from a single 3.3 V power supply and has a low 366 mW power consumption at 80 Msps. The sample-to-hold amplifier (SHA) input maintains excellent performance for input frequencies up to 100 MHz and is configured as single-ended in this application. A single-ended clock input was used to control all the internal conversion cycles provided by FPGA. A clock duty cycle stabilizer (DCS) was used to re-time the non-sampling edge and provide an internal clock signal with a nominal 50% duty cycle. This allows for a wide range of clock input duty cycles without affecting the performance of AD9236. Hence, additional single-ended-to-differential circuits or clock sources are not required. Using an internal reference voltage, the circuit design can be simplified. Finally, the digitalized signals were delivered to the Spartan-7 FPGA (XC7S25-1CSGA324C, Xilinx), where a critical discrimination algorithm was implemented. The FPGA must perform three main tasks: provide the clock source for the ADC, receive and process the digitized signal from the ADC, and upload the energy spectra. Digital circuits require voltages of 1.0V, 1.8V, and 3.3V. These low voltages were generated using low-dropout (LDO) linear regulators (TLV74110, TLV74118, TLV75533, TI). These LDO regulators have fixed output voltages and their peripheral circuits require only capacitors for filtering.

The PSD algorithm was implemented using several modules on FPGA. The digital antinoise filter and signal preprocessing module use FIFO to cache the data from the ADC. Furthermore, they filter the high-frequency noise and adjust the pulse shape when severe pulse undershoot occurs. Instead of being sent directly to the discrimination module, the filtered signals are first processed using a trapezoidal pulse shaper. The trapezoidal pulse shaper is conducive to magnifying the difference between neutron and gamma signals. Its low computational complexity makes the real-time discrimination of FPGA easy to achieve. The input and output signals of the trapezoidal shaper are processed separately in two parallel modules. One module is the n/γ discrimination module, which identifies signal types by analyzing the characteristics of the shaped signals, and the other is the peak extraction module, which selects the maximum amplitude from the pulse data in the duration of the original signals. Consequently, with the identified signal types and amplitudes, the spectrum formation module forms gamma spectra, neutron response spectra, and PSD plots, which

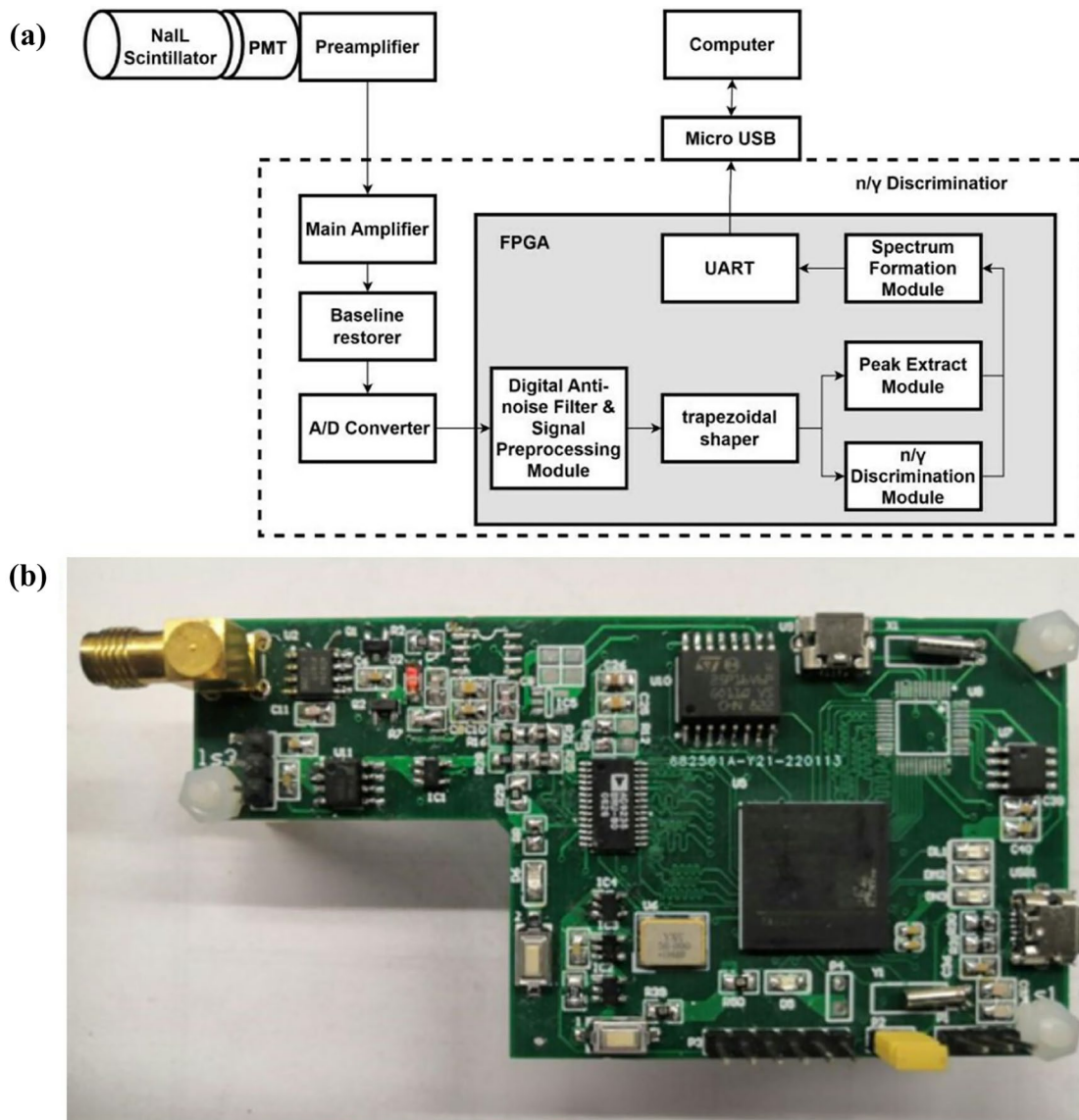


Fig. 1 (Color online) **a** Block schematic of the real-time digital pulse shape discriminator. **b** Real-time digital pulse shape discriminator

are updated in real-time after a new pulse signal arrives. Owing to the low power consumption of the discriminator and the small amount of spectrum data, only one USB port is required for power supply and data transmission.

2.2 Pulse-shaping technique

In the radiation detection system, RC-CR circuits and a Sallen-Key filter were used to filter out noise from the amplified nuclear signals to obtain an optimum signal-to-noise ratio (SNR). These filters remove the high-frequency components in the frequency domain, causing a change in the shape of the signals in the time domain. For example, RC-CR circuits and a Sallen-Key filter can process a signal

into a Gaussian-like shape in both analog and digital ways [26–28]. In addition to filtering, the signals must be specifically shaped to accommodate different application scenarios. The signal should be narrow at high count rates and have a flat top for amplitude analysis. In time analysis, steepening the leading edge of the signals makes the timing accurate. Using the digital pulse-shaping technique, a digital shaper can meet diverse requirements and process signals into a variety of shapes, such as trapezoidal and triangular.

A trapezoidal pulse-shaping algorithm was developed using the z -transform method [29]. The z -transform method comprises two main steps. The first step is to acquire the transfer function $H(z)$ through the z -transformation of the input and output signals. The next step is to apply an inverse

z-transform to obtain the equations for the input and output signals in the time domain.

Common signal-processing algorithms, such as fast Fourier transform (FFT) and finite impulse response (FIR) filters, require numerous multiplication and addition operations. Moreover, the internal DSP slices of the FPGA can conveniently perform basic multiplication and addition operations. As shown in Fig. 2a, the trapezoidal pulse-shaping algorithm derived from the z-transform method could be implemented as a shaper in FPGA. Because this algorithm requires high-precision multiplication and addition operations, the adders and multipliers should have large bit widths. This algorithm also requires additional operations to remove the baseline drift caused by noise accumulation [29].

Another method of achieving a digital trapezoidal shaper is the unfolding synthesis technique. Because of the limitations of the bit width, hardware resources, and real-time processing requirements, a trapezoidal shaper should be

simple and efficient for FPGA. The unfolding technique was introduced to transform digital signals from an ADC into a unit impulse, which can approximately synthesize any pulse shape [17]. The nuclear signal amplitude increased rapidly to a maximum value and then decayed at a relatively slow rate. For NaI:Tl crystals, the decay time of light output has both fast and slow components [30]. The current signal output from the PMT was converted into a voltage pulse in the resistive feedback preamplifier followed by an RC network. Figure 3a shows the digitalized voltage pulse, which can be expressed as:

$$V[n] = A \left(e^{-\frac{n}{\tau_1}} - e^{-\frac{n}{\tau_2}} \right), \tag{1}$$

where τ_1 and τ_2 represent the decay time constants of the digital signal in a bi-exponential shape, which includes the preamplifier time constant, scintillation fluorescence time constant, electronic characteristics of the anode, and

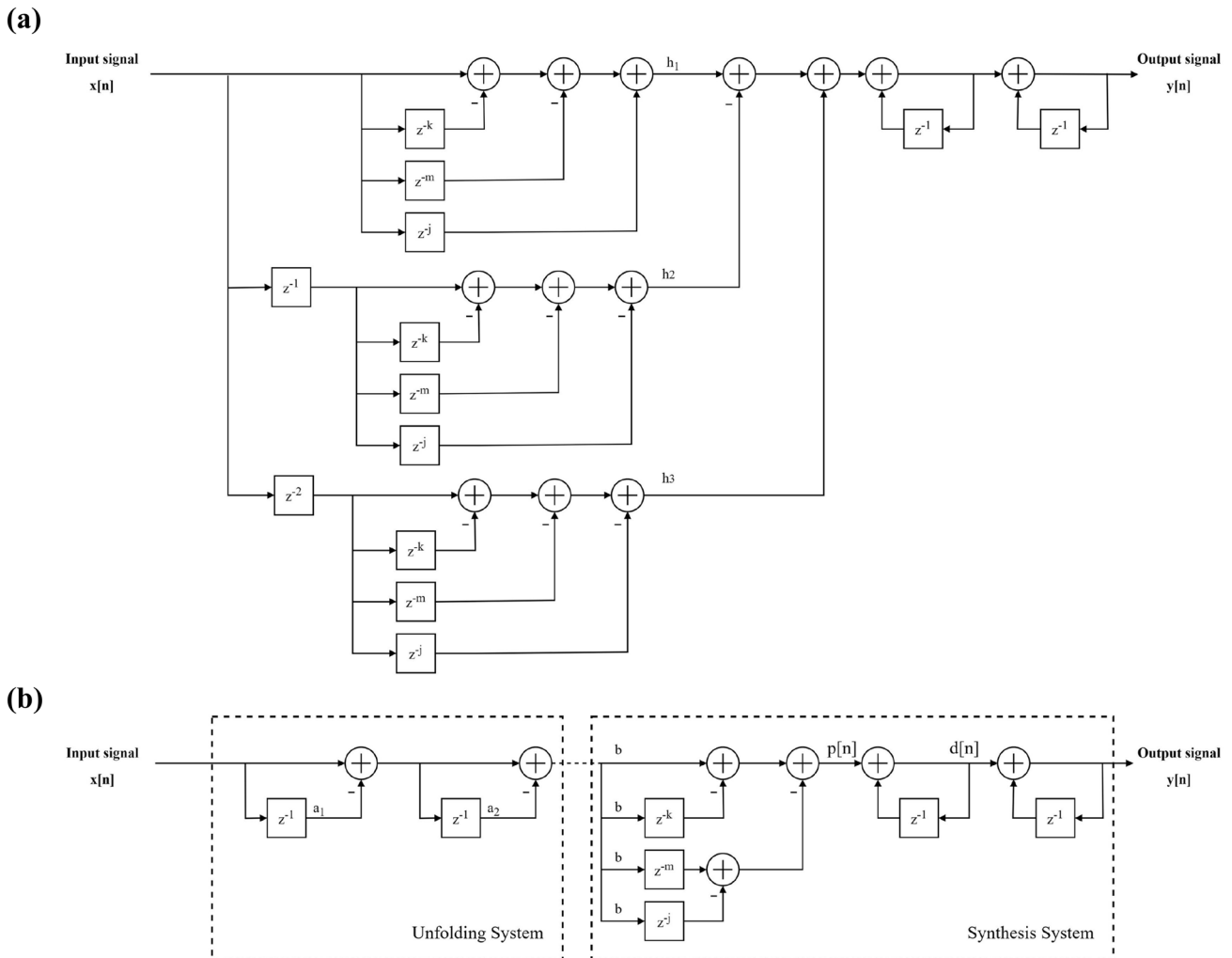


Fig. 2 **a** Functional block diagram of the trapezoidal shaper using the z-transform method. **b** Functional block diagram of the trapezoidal shaper using unfolding synthesis technique

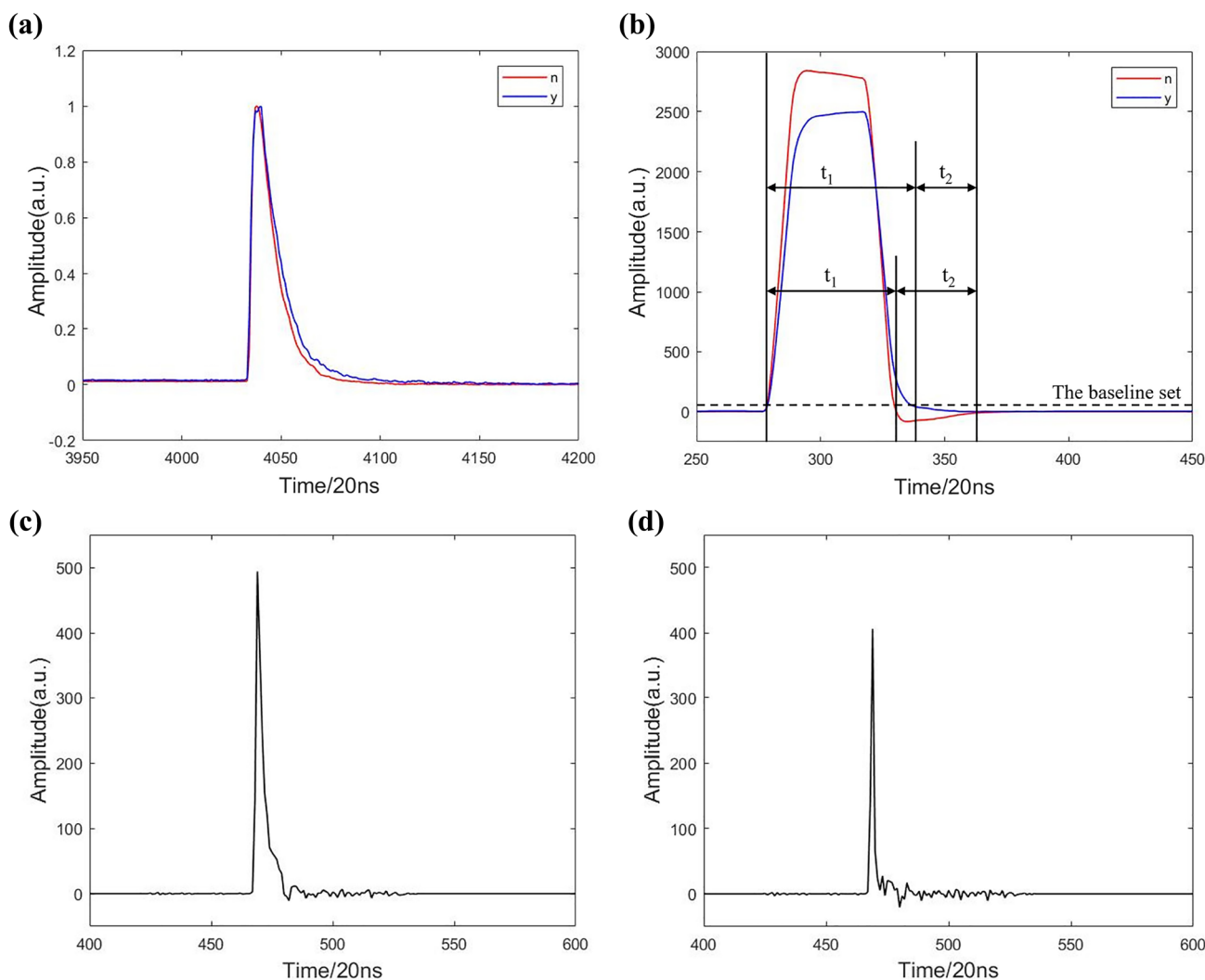


Fig. 3 **a** Averaged gamma-ray and neutron pulses from the NaIL detector. **b** Illustration of the PSD algorithm based on the trapezoidal shaper. **c** First signal deconvolution of the input signal when a_1 is

0.9048. **d** Second signal deconvolution of the input signal when a_1 is 0.9048 and a_2 is 0.7515

preamplifier-anode coupling. A indicates the pulse amplitude and also controls the signal width. The interval between two adjacent sampling points n is determined by the sampling rate. Equation (1) serves as a fitting model to obtain the decay time constants of the digital pulse.

Because the output signal of the detector has a bi-exponential shape, the first step is to deconvolute the bi-exponential signal into a unit impulse $\delta[n]$. The operational algorithm of a system that unfolds an exponential unit impulse response is given by the following equation [17]:

$$\delta[n] = x_N[n] - a \cdot x_N[n - 1]. \tag{2}$$

There is also a double-exponential impulse-shaping algorithm for obtaining a narrower δ signal, which might result in better anti-pile-up applications [31]. All deconvolution

methods produce an approximate δ signal that retains time and amplitude information. The difference between these methods lies in the width of the δ signal and complexity of the algorithm. Although Eq. (2) is derived for a single exponential pulse, good shaping results can be obtained by using Eq. (2) twice. Figure 3c, d shows that the signal becomes significantly narrower and smaller after two deconvolutions.

The next step was to synthesize a unit pulse using a trapezoidal pulse. The operational algorithm for the synthesis system was deduced from the shape of the target waveform. A standard trapezoidal pulse can be described as

$$y[n] = \begin{cases} \frac{A}{k} & n < k \\ A & k \leq n \leq m \\ -\frac{A}{k} \cdot n + \frac{A}{k} \cdot (2 \cdot k + l) & x > m \end{cases} \quad (3)$$

After differentiating the primary function $y[n]$, the function value of each interval becomes constant, resulting in $d[n]$

$$d[n] = \begin{cases} \frac{A}{k} & n \leq k \\ -\frac{A}{k} & m \leq n \leq j \end{cases} \quad (4)$$

The weighted and shifted unit impulses can be used to represent the differentiation of $y[n]$. Therefore, an alternative expression for $d[n]$ is as follows:

$$d[n] = \frac{A}{k} \cdot (u[n] - u[n - k]) - \frac{A}{k} \cdot (u[n - m] - u[n - j]) \quad (5)$$

$\delta[n]$ is the result of the difference operation of $u[n]$, and the synthesis system based on recursive difference equations in the time domain [32, 33] is given as follows:

$$p[n] = \frac{A}{k} \cdot (\delta[n] - \delta[n - k]) - \frac{A}{k} \cdot (\delta[n - m] - \delta[n - j]), \quad (6)$$

$$d[n] = p[n] + d[n - 1], \quad (7)$$

$$y[n] = d[n] + y[n - 1], \quad (8)$$

where k is the duration of the rising/falling edge of the trapezoidal pulse and $|m - j|$ is the duration of the flat time of the trapezoidal pulse. $|m - j|$ and k could be large enough so that the signal has enough time to rise to its maximum amplitude, thus compensating for the ballistic deficit effect [34]. However, a long signal duration causes pile-up events when the count rate is high, which is unhelpful for n/γ discrimination. In this study, we did not consider the pile-up situation. Thus, we can only discard pile-up events by determining whether there are multiple peaks in the pulse duration. The tail pile-up pulses could be separated when only counting was considered. However, when a neutron pulse and gamma pulse are stacked together, it is difficult to separate them while retaining their distinct original features. The challenge of separating the neutron and gamma signal pile-ups remains. Therefore, the parameters of the algorithm were set to prevent the shape of the trapezoidal signal width from exceeding the original signal width. Figure 2(b) shows the block diagram of the trapezoidal shape algorithm. The parameter b is the amplitude factor that controls the digital gain. The parameters a_1 and a_2 are determined by the decay time constant τ and sample period ΔT :

$$a_1 = e^{-\Delta T/\tau_1}, \quad (9)$$

$$a_2 = e^{-\Delta T/\tau_2}. \quad (10)$$

In Fig. 2, compared with the z -transform method, the trapezoidal shaper derived from the idea of unfolding synthesis technique has fewer adders and multipliers. In reality, fewer operations of the trapezoidal shaper are attributed to the deconvolution of the digital pulse. Signal deconvolution shifts the target of the trapezoidal shape from a bi-exponential signal to a δ signal that retains the energy information of the original signal [35]. The implementation of signal deconvolution reduces baseline shifts at high count rates and improves energy resolution [35, 36]. Hence, fewer operations do not necessarily result in poor performance. The recursive method for the trapezoidal shaper using Eqs. (2), (6), (7), and (8) is shown in Fig. 2(b).

2.3 PSD algorithm based on a trapezoidal shaper

The digitalized neutron and gamma signals sampled from the ADC are shown in Fig. 3a. Neutron and gamma waveforms were normalized to the same area for comparison with the same gamma-equivalent energy. We consider the rise time as the time when a signal crosses from a specific low-voltage threshold to a specific upper-voltage threshold (10–90%), and the fall time as 90% to 10% of the signal tail. The rise time of the gamma signal was 58 ns and its fall time was 470 ns. The rise and fall times of the neutron signals were 46 and 413 ns. The two signals in Fig. 3a could be fitted using a bi-exponential function. The fast component of the gamma signal was 70 ns and its slow component was 200 ns. The fast and slow components of the neutron signal were 64 and 160 ns. It is evident that the neutron and gamma signals have different decay time constants. The difference between the two signals appears to be small when viewed by the human eye. It can be presumed that the results obtained after integrating the signals directly will also be similar. The use of a trapezoidal shaper avoids the direct processing of similar original signals and analyzes the new features of the shaped signals. Because parameters a_1 and a_2 are set for gamma signals, the trapezoidal shaper does not match the neutron signals. Thus, the two types of signals formed different shapes, as shown in Fig. 3b. The gamma signal is shaped into an approximate trapezoidal signal, whereas the output of the neutron signal has the characteristics of overshoot and undershoot owing to the unmatched parameters a_1 and a_2 . According to the output characteristics of the neutron signals from the trapezoidal shaper, the n/γ and peak extraction modules cooperate in the following states:

- (1) t_1 denotes the time at which the signal amplitude exceeds the baseline value. During time t_1 , the max-

imum value of the original signals is determined through successive comparisons and recorded.

- (2) The time t_2 from when the signal decays to the baseline until it returns to zero is recorded.
- (3) After completing the record of t_2 , the peak value is sent to the spectrum formation module to identify whether the peak value belongs to the neutron response spectrum or the gamma spectrum by calculating the correlation factor λ :

$$\lambda = t_1 / (t_1 + t_2). \quad (11)$$

λ takes values between 0 and 1, and it characterizes the magnitude of the undershoot and the overshoot of the signal. When the neutron pulse signal width is relatively narrow, the signal decays quickly causing an undershoot and resulting in a long t_2 and short t_1 for peak extraction. Typically, λ of the neutron signal is smaller than that of the gamma signal, which means that the neutron peak is on the left side of the gamma peak in the PSD plot.

Low sampling rates affect the trapezoidal shaping results, but more importantly, they result in inaccurate measurements of t_1 and t_2 . Owing to the low-sampling-rate requirement of the shaper and the amplification of the difference between the neutron and gamma signals, this algorithm is characterized by its ability to work at low sampling rates compared to some mainstream algorithms [22].

The neutron and gamma signals were processed in the same trapezoidal shaper and shaped into a nonstandard trapezoidal pulse. In Fig. 3b, although the output of the gamma signal has a relatively flat top, the output of the neutron signal has an uneven top that could shift the neutron response peak to the right in energy analysis. Thus, using the parallel-processing capabilities of the FPGA, the peak extraction module matches the peaks of the original signals to the shaped signals.

3 Experimental setup

A $\Phi 50.8 \text{ mm} \times 50.8 \text{ mm}$ ^6Li -enriched (95%) NaI:Tl scintillator with 1% ^6Li doping was chosen because it has a high light output yield exceeding 30000/MeV [6]. A preliminary check of the detector response to gamma rays was performed using a ^{137}Cs gamma source. The energy resolution was 7.01% at 662 keV. The experiments were implemented using a 30 mCi $^{241}\text{Am-Be}$ neutron source. Thermal neutrons were indirectly detected through $^6\text{Li}(n, \alpha)^3\text{H}$ reaction, which emitted ^3H and α particles with a total energy of 4.79 MeV. Only part of the energy was deposited in the NaI:Tl, ^6Li crystal because of the luminous efficiency of α and ^3H particles [37]. The cross section of the thermal neutron capture on ^6Li was 940 b. A major

advantage of using ^6Li to capture neutrons is that the reaction has a high reaction energy, and a neutron response energy of 4.79 MeV can be easily distinguished from the gamma background. Additionally, discrimination between the neutron and gamma signals in the low-energy region can be avoided using the nuclear reaction method.

The count rates can differ when the distance between the $^{241}\text{Am-Be}$ source and the detector varies. The count rate of gamma rays and neutrons was 1.8 kcps when the distance was set to 20 cm with a 6-mm-thick lead shield, and 22 kcps without a lead shield. The $^{241}\text{Am-Be}$ source was placed 20 cm away from the detector with a 6-mm-thick lead shield for moderate reduction of the gamma background. Four arrangements were used to determine the appropriate PSD parameters and evaluate the pulse shape discrimination ability of the discriminator.

The trapezoidal shaper is completed in the first part. The waveforms of digitalized signals were extracted using an integrated logic analyzer. By fitting the neutron and gamma signals with a bi-exponential function, we can obtain approximate decay time constants to build a trapezoidal shaper. After loading the original pulse data from the integrated logic analyzer into the MATLAB workspace, a shaper was built and simulated in Simulink of MATLAB. The decay time constants obtained by fitting with a bi-exponential function were float-point-type constants. To enhance the operation speed and save data memory in FPGA, all parameters were converted into a fixed-point type. The output results of each operation were rounded and saturated on an integer overflow because of the limitation of fixed-point precision. This is why the precision of the algorithm in FPGA decreases as the operations increase and the final shaping results are not as accurate as the theoretical calculation. An inaccurate operation output can cause a baseline shift and pulse shape distortion. The algorithm operations were most likely halted when an overflow occurred. One way to solve these problems is to control the value and bit width of the operation results and parameters, such as a_1 , a_2 , and b . Because shaped signals can be observed in real time using an integrated logic analyzer, the parameters of the algorithm were manually adjusted after observation. Each adder, multiplier, and accumulator in FPGA were also set to have different output bit-width limitations.

The second part tested whether the algorithm could make signals distinctive and whether the spectrum formation module worked to form a PSD plot. The trapezoidal shaper was implemented in the discriminator to complete the neutron/gamma discrimination algorithm. The spectrum formation module in FPGA was selected to record the PSD plot. The discriminator sampled the neutron and gamma signals for some time to acquire PSD plots, which demonstrated different λ values for all counts.

Neutron and gamma peaks are observed in the PSD plot. Assuming that the peaks follow a Gaussian distribution, we use a figure of merit (FoM), defined as

$$\text{FoM} = \frac{S}{\text{FWHM}_\gamma + \text{FWHM}_n}, \quad (12)$$

to determine the quality of discrimination.

S denotes the distance between the neutron response and gamma peaks, while FWHM_γ and FWHM_n represent the full widths at half maximum of the corresponding peaks. The FoM is high when there are few statistical fluctuations; the two peaks are significantly separated, and a high FoM indicates a good discrimination ability. According to the PSD plot, the neutron signals can be distinguished if λ is smaller than a threshold, $\lambda_{\text{standard}}$. After $\lambda_{\text{standard}}$ was determined and set in FPGA, the spectrum formation module was modified to form two-pulse amplitude spectra.

Subsequently, the determined parameters and modified modules in FPGA were used to acquire the final spectra in the third part. For instance, in the experiment at a 50 MHz sampling rate, $a_1 = 0.9048$, $a_2 = 0.7515$, $b = 1.5$, $k = 10$, $|m - j| = 20$, and $\lambda_{\text{standard}} = 0.45$. The signals were classified as neutron signals when λ was < 0.45 . In this section, two 4096 channel spectra are uploaded from FPGA to a computer every 2 s. These parameters were set manually beforehand and could be fixed for the current experimental conditions. Changes in the source intensity, detector type, and detector location from the source might invalidate these parameters and deteriorate the discrimination quality. Therefore, the experimental steps described above must be repeated to obtain the best parameters when the detection conditions change. The fourth part is the shielding experiment conducted in the previous two parts. A 1.5-mm-thick cadmium plate was used to absorb neutrons, which allowed us to compare the discrimination efficiency and ensure that only a few neutron signals were omitted.

4 Results and discussion

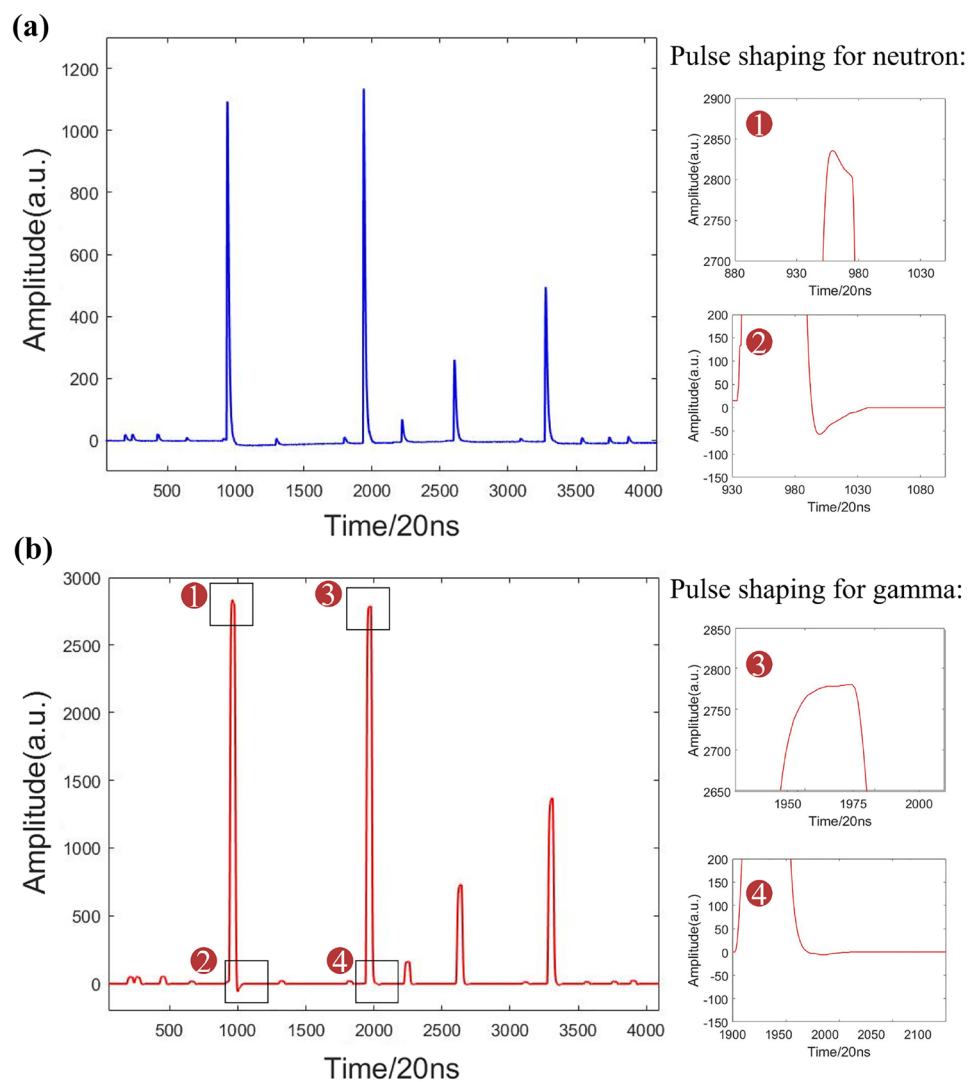
As discussed previously, a PSD discriminator and its embedded algorithm were designed and implemented. Without lead shielding, several input and output signals from the trapezoidal shaper were captured using an integrated logic analyzer. With 6 mm lead shielding, the probability of pile-up events occurring was reduced. The presence of massive low-energy gamma rays results in many low-amplitude pulses, as shown in Fig. 4a. The signal shapes, with pulse widths shorter than 2 μs , are shown in Fig. 4b. A gamma signal with a large amplitude was deliberately acquired. After trapezoidal shaping, the gamma signals feature a flat top, whereas the neutron signals exhibit an overshoot at the top. The gamma

and neutron signals exhibit small and severe undershoots, respectively. Thus, a signal with an amplitude of 2836 can be identified as a neutron signal by the evident overshoot and undershoot. In Fig. 4a, the neutron signal has a shorter decay time and high amplitude and already has a minor undershoot before pulse shaping. This can be eliminated by an analog circuit of pole-zero cancelation, which was not used in this experiment, considering the remaining original difference in the output signals of NaI:Tl and ^6Li detectors. The fast decay of the neutron signal causes a baseline drift in the signal after the neutron signal. However, in Fig. 4b, the neutron signal is restored to the baseline relatively quickly after pulse shaping. The signal after the neutron signal was less affected by the baseline drift. This demonstrates the ability of the pulse-shaping technique to achieve pile-up decomposition. Fast shapers can shorten the rise and fall times of signals, reducing the occurrence of tail pile-up events. The shaped-signal width can be narrowed by adjusting the parameters of the trapezoidal shaper or using a cusp shaper. For example, a flat top can be eliminated when $|m - j|$ is set to zero, and the signal is processed into a triangular shape with a short signal width.

The quality of discrimination using the pulse-shaping method with the NaI:Tl, ^6Li detector is shown in Fig. 5. These plots were uploaded directly to the FPGA. The distribution of counts with a correlation factor λ approximates a Gaussian distribution, and there is a wide gap between the two peaks. The left peak is the neutron response peak, whereas the right peak is the gamma peak due to the large number of low-energy gamma rays. The left peak disappeared after adding a 1.5-mm-thick cadmium plate, proving that the left peak was a neutron response peak. The right peak was taller in Fig. 5b than in a, which also implies that cadmium has a high (n, γ) reaction cross section [38] and accordingly produces more gamma rays. Setting a threshold of 50 allowed an energy measurement from 57.195 keV to 5.695 MeV, which covered the energy range of the neutron response. Additionally, setting a threshold taller than 0 helps filter out unconcerned low-amplitude noise. In one minute, the FoM is 2.88 at a 50 MHz sampling rate allowing for the determination of the sound parameters, which is sufficient for efficiently separating the neutron and gamma signals. This effective separation was attributed to the unique shape difference between the gamma and neutron pulses amplified by the trapezoidal shaper.

Moreover, the signals can be discriminated at lower sampling rates using suitable parameters. We set a_1 to 0.8825, a_2 to 0.6997, and $\lambda_{\text{standard}}$ to 0.45 for a sampling rate of 40 MHz. We set a_1 to 0.8187, a_2 to 0.5647, and $\lambda_{\text{standard}}$ to 0.4 for a sampling rate of 25 MHz. The width of the trapezoidal pulse remained constant. An increase or decrease in the sampling rate did not affect the inherent decay time of the signal. From Eq. (9) and Eq. (10),

Fig. 4 **a** Amplified signals from the NaIL detector. **b** Pulse shaping of mixed neutron-gamma signals



we deduce that changes in the sampling rate affect a_1 and a_2 , and alter the results of the trapezoidal shaper. The fall time of the neutron signal was 413 ns, and there were no more than 24 sampling points on the falling edge when the sampling rate was 50 MHz. After the sampling rate was reduced to 25 MHz, there were no more than 12 sampling points at the falling edge of the neutron signal. Similarly, there were fewer than three sampling points at the rising edge. Sometimes, only one sampling point was observed during the signal rise time. Thus, owing to the short duration of a nuclear signal, a low sampling rate affects the fidelity of digitalized signals. Although the trapezoidal shaper still operates normally at a 25 MHz sampling rate, the number of sampling points available for calculating λ is reduced by half at a 25 MHz sampling rate compared to a 50 MHz sampling rate, which makes λ less accurate. As shown in Fig. 5e, the inaccuracy of λ broadens the bottom of the peak and increases the distance between the two peaks. The dispersion of the counts makes the

FWHM narrower. Therefore, the FoM values calculated using Eq. 12 are higher. The results show great discrimination ability at lower sampling rates when only counting is considered, but the quantization error caused at a 25 MHz sampling rate could deteriorate the energy measurements. Therefore, peak extraction should be applied to the original or output signals of the other shapers.

The sampling rate is not the main factor affecting the FoM value but a constraint of the pulse discrimination method. In some methods, the scale of the sampling rate has certain requirements for computational accuracy. The adaptability of the method described above allows discrimination over a wide range of sampling rates. The parameter selection of the trapezoidal shaper largely determines the discrimination performance of the method. The decay time constants of the output signals of the different detectors were not the same. Therefore, this pulse-shaping method must fit the digitalized signals of the ADC in advance to obtain the approximate decay time constants.

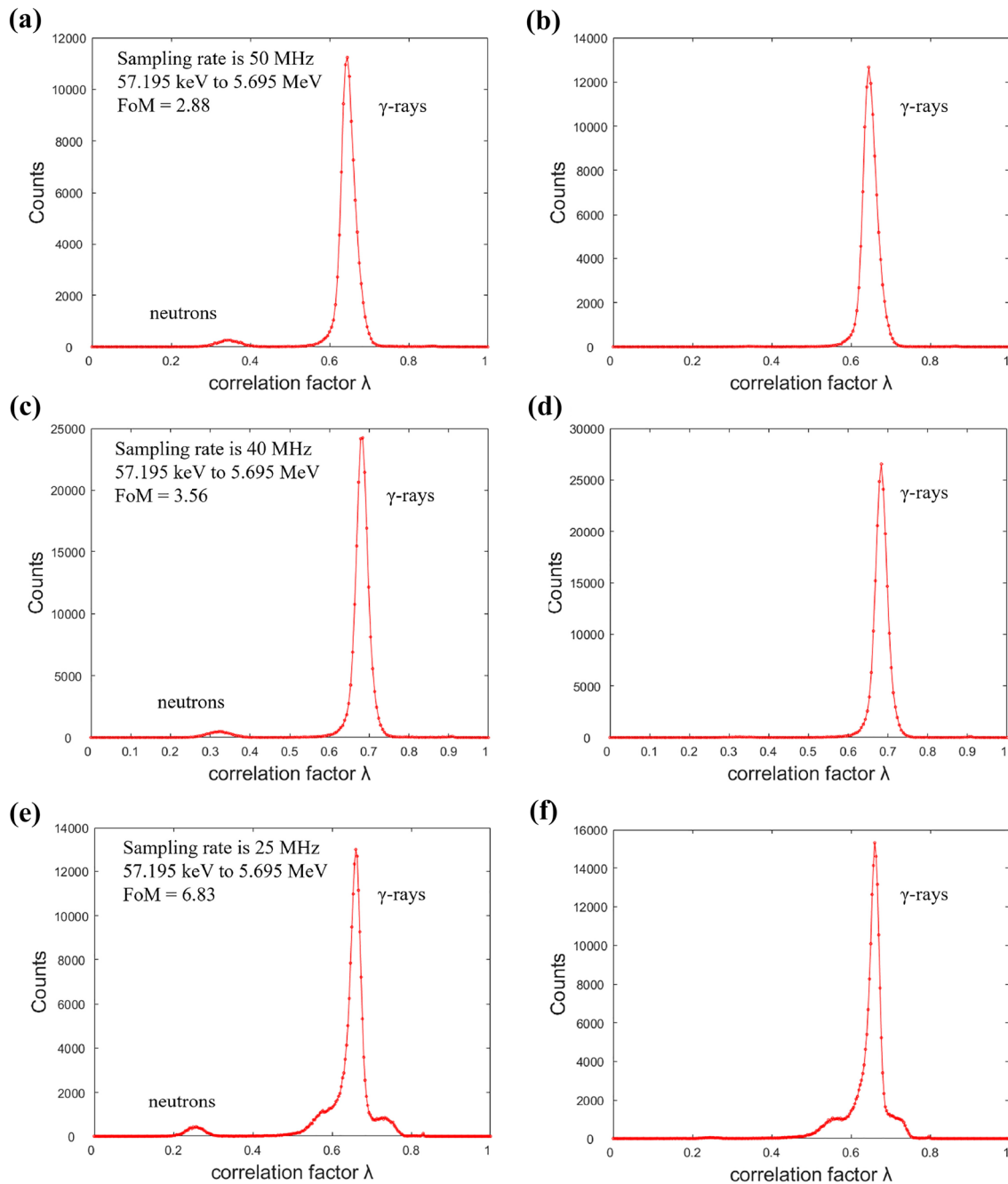


Fig. 5 PSD plot obtained at a 50 MHz sampling rate (a) without and (b) with cadmium shielding. PSD plot obtained at a 40 MHz sampling rate (c) without and (d) with cadmium shielding. PSD plot obtained at a 25 MHz sampling rate (e) without and (f) with cadmium shielding

The neutrons emitted by the ^{241}Am -Be source were not monoenergetic. The main reason why the neutron spectrum is continuous is the continuous energy of α particles produced by the α decay of ^{241}Am [39]. Additionally, the energy loss of α particles exists owing to the collisions of α particles with target nuclei and Coulomb repulsion interaction. Nevertheless, the reaction products directly

transitions from the excited state to the ground state and the energy transferred to the reaction products is uniquely determined. The total energy of 4.79 MeV emitted from $^6\text{Li}(n, \alpha)^3\text{H}$ reaction is carried by ^3H and α particles, when the kinetic energy of the neutrons is neglected. This energy is the response of thermal neutrons and thus should exhibit a single-peak distribution at the energy of 4.79 MeV in the energy spectrum. For different scintillators, the luminous

efficiencies of ^3H and α particles were different for the different scintillators. In this experiment, the response energy deposited in the NaI:Tl, ^6Li detector was assumed to be less than 4.79 MeV.

Before implementing the PSD algorithm, we plotted Fig. 6a, b based on the mixed neutron-gamma radiation field for a measurement time of 2 min. The gamma-ray peak with the highest energy is the full energy peak of 4.438 MeV emitted from the $^9\text{Be}(\alpha, n)^{12}\text{C}^*$ reaction [40]. Subsequently, a single-escape peak occurred at 3.927 MeV and a double-escape peak occurred at 3.416 MeV. The ^{241}Am -Be neutron source was surrounded by boron-containing polyethylene plates that were used to prevent neutron leakage. Therefore, neutrons are captured by hydrogen in boron-containing polyethylene, which leads to a gamma-ray peak at an energy of 2.23 MeV. Moreover, ^{10}B is a suitable material for shielding neutrons from $^{10}\text{B}(n, \alpha)^7\text{Li}^*$

reactions. The ^7Li in the excited state quickly deexcites to its ground state and emits gamma rays with 478 keV energy. Relying on the high thermal neutron absorption cross section of Cd, the two spectra were combined to confirm the energy range of the neutron response. The area marked in red indicates the response energy range of the thermal neutrons that occur near the single-escape peak of ^{12}C .

After implementing the PSD algorithm, we plotted Fig. 6c, d, which show the separated spectra uploaded from the discriminator to the computer. The response peak for the reaction of thermal neutrons with ^6Li lies at an energy of 3.9 MeV. The successful extraction of the neutron response spectrum indicates that neutron signals with different amplitudes can be discriminated. Although the pulse width increased with the pulse amplitude, the pulse amplitude did not affect the intrinsic decay time constant. Accordingly,

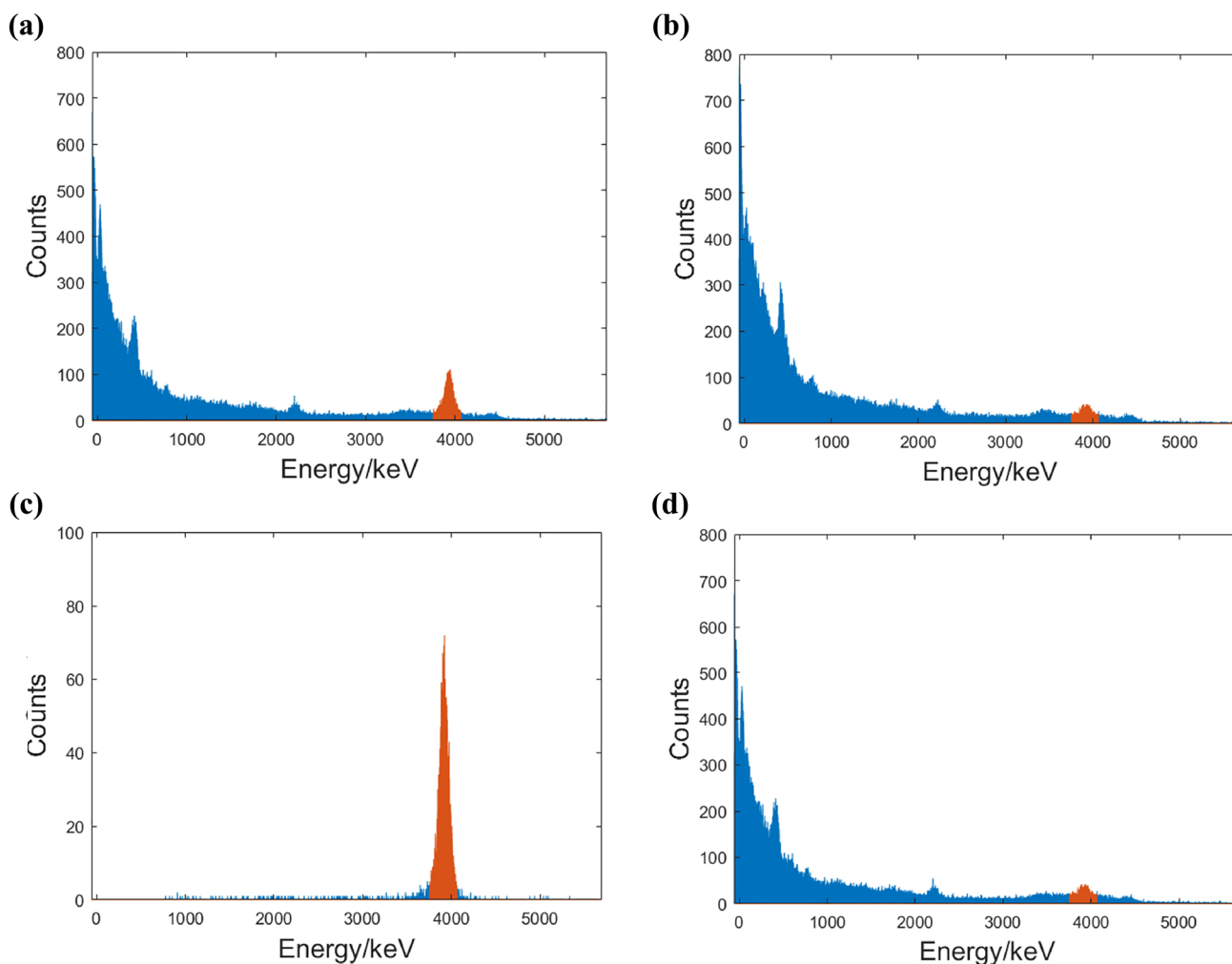


Fig. 6 Response spectrum of mixed neutron and gamma signals not using the PSD algorithm (a) without and (b) with cadmium shielding. (c) Neutron response spectrum and (d) gamma spectrum obtained using the PSD algorithm without cadmium shielding

changes in the signal amplitude do not affect the recognition of the neutron signals. The separated gamma-energy spectra shown in Fig. 6d are similar to those in Fig. 6b, but the counts will be higher in low-energy areas with cadmium shielding owing to the $^{113}\text{Cd}(n, \gamma)$ reaction. Then, we compare the red peak area in the four spectra, which is the energy range from 3.75 to 4.07 MeV. The total counts in the energy range with the gamma and neutron signals in Fig. 6c are 9987, and the counts reduce to 4903 when neutrons are shielded by cadmium. The peak areas of Fig. 6c, d are 5149 and 4755, respectively. Their sum corresponds to the total counts of the spectrum in Fig. 6a, which indicates that the pulse-shaping method does not cause significant count loss.

5 Conclusion

A portable n/γ discriminator and its embedded algorithm were tested at low sampling rates. The results showed satisfactory PSD performances of the NaI:Ti, ^6Li scintillator and discriminator. This method can also be used for other gamma-ray and neutron dual-detection scintillators, such as CLYC and CLLB. Unlike sophisticated computer-based PSD methods, the low cost, low sampling rate, and real-time processing have significant advantages in practical applications. Future investigations into the application of this simple but robust discrimination method to the assembly of scintillator array and SiPM array are of particular interest. In radiation imaging applications, using n/γ dual-detection scintillator arrays with this method can simultaneously and effectively obtain neutron and gamma images, thereby reducing the size and cost of the imaging instruments.

Author contributions All authors contributed to the study conception and design. Material preparation, data collection, and analysis were performed by Jia-Xin Li and Hui-Liang Hou. The first draft of the manuscript was written by Jia-Xin Li and all authors commented on previous versions of the manuscript. All authors read and approved the final manuscript.

Data availability The data that support the findings of this study are openly available in Science Data Bank at <https://www.doi.org/10.57760/sciencedb.10886> and <https://cstr.cn/31253.11.sciencedb.10886>.

Declarations

Conflict of interest The authors declare that they have no competing interests.

References

- F. Zhang, Q. Zhang, R.P. Gardner et al., Quantitative monitoring of CO_2 sequestration using thermal neutron detection technique in heavy oil reservoirs. *Int. J. Greenh. Gas. Con.* **79**, 154–164 (2018). <https://doi.org/10.1016/j.ijggc.2018.10.003>
- C. Lynde, C. Frangville, R. Woo et al., On the use of pixelated plastic scintillator and silicon photomultipliers array for coded aperture gamma-neutron imaging. *IEEE Trans. Nucl. Sci.* **69**, 731–737 (2022). <https://doi.org/10.1109/TNS.2022.3140601>
- D. Vanderwerken, M. Millett, T. Wilson et al., Meteorologically driven neutron background prediction for homeland security. *IEEE Trans. Nucl. Sci.* **65**, 1187–1195 (2018). <https://doi.org/10.1109/TNS.2018.2821630>
- R.T. Kouzes n, A.T. Lintereur, E.R. Siciliano, Progress in alternative neutron detection to address the helium-3 shortage. *Nucl. Instrum. Methods A* **853**, 27–35 (2017). <https://doi.org/10.1016/j.nima.2017.02.022>
- C.L. Wang, L.L. Funk, R.A. Riedel et al., Improved neutron-gamma discrimination for a ^3He neutron detector using subspace learning methods. *Nucl. Instrum. Methods A* **784**, 172–175 (2015). <https://doi.org/10.1016/j.nima.2014.10.046>
- K. Yang, P.R. Menge, V. Ouspenski, Li co-doped NaI:TL (NaIL)-a large volume neutron-gamma scintillator with exceptional pulse shape discrimination. *IEEE Trans. Nucl. Sci.* **64**, 2406–2413 (2017). <https://doi.org/10.1109/TNS.2017.2721398>
- Z. Zuo, Y.L. Xiao, Z.F. Liu et al., Discrimination of neutrons and gamma-rays in plastic scintillator based on falling-edge percentage slope method. *Nucl. Instrum. Methods A* **1010**, 165483 (2021). <https://doi.org/10.1016/j.nima.2021.165483>
- E.V. Ryabeva, I.V. Urupa, E.E. Lupar et al., Calibration of EJ-276 plastic scintillator for neutron-gamma pulse shape discrimination experiments. *Nucl. Instrum. Methods A* **1010**, 165495 (2021). <https://doi.org/10.1016/j.nima.2021.165495>
- H.R. Liu, Y.X. Cheng, Z. Zuo et al., Discrimination of neutrons and gamma-rays in plastic scintillator based on pulse coupled neural network. *Nucl. Sci. Tech.* **32**, 82 (2021). <https://doi.org/10.1007/s41365-021-00915-w>
- X. Pang, Z. Zhang, J. Zhang et al., A compact MPPC-based camera for omnidirectional (4π) fast-neutron imaging based on double neutron-proton elastic scattering. *Nucl. Instrum. Methods A* **944**, 162471 (2019). <https://doi.org/10.1016/j.nima.2019.162471>
- T. Yanagida, K. Watanabe, Y. Fujimoto, Comparative study of neutron and gamma-ray pulse shape discrimination of anthracene, stilbene, and p-terphenyl. *Nucl. Instrum. Methods A* **784**, 111–114 (2015). <https://doi.org/10.1016/j.nima.2014.12.031>
- X. Wen, A. Enqvist, Pulse shape discrimination of $\text{Cs}_2\text{LiYCl}_6:\text{Ce}^{3+}$ detectors at high count rate based on triangular and trapezoidal filters. *Nucl. Instrum. Methods A* **866**, 129–133 (2017). <https://doi.org/10.1016/j.nima.2017.06.007>
- K. Li, X. Zhang, Q. Gui et al., Characterization of the new scintillator $\text{Cs}_2\text{LiYCl}_6:\text{Ce}^{3+}$. *Nucl. Sci. Tech.* **29**, 11 (2018). <https://doi.org/10.1007/s41365-017-0342-4>
- H. Singh, R. Mehra, Discrete wavelet transform method for high flux $n-\gamma$ discrimination with liquid scintillators. *IEEE Trans. Nucl. Sci.* **64**, 7 (2017). <https://doi.org/10.1109/TNS.2017.2708602>
- J.W. Wang, W.G. Gu, H. Yang et al., Analytical method for γ energy spectrum of radioactive waste drum based on deep neural network. *Nuclear Techniques* **45**(4), 040501 (2022). <https://doi.org/10.11889/j.0253-3219.2022.hjs.45.040501>. (in Chinese)
- V.T. Jordanov, K.V. Jordanova, Unfolding-synthesis technique for digital pulse processing. *Nucl. Instrum. Methods A* **1004**, 167421 (2022). <https://doi.org/10.1016/j.nima.2022.167421>
- V.T. Jordanov, Unfolding-synthesis technique for digital pulse processing. Part 1: unfolding. *Nucl. Instrum. Methods A* **805**, 63–71 (2016). <https://doi.org/10.1016/j.nima.2015.07.040>
- B. Blair, C. Chen, A. Glenn et al., Gaussian mixture models as automated particle classifiers for fast neutron detectors. *Stat. Anal. Data Min.* **12**, 479–488 (2019). <https://doi.org/10.1002/sam.11432>

19. S. Qi, J. Li, S. Wang et al., Online neutron/gamma discrimination and source detection using CLYC(Ce) scintillator: a sequential approach. *Nucl. Instrum. Methods A* **1014**, 165733 (2021). <https://doi.org/10.1016/j.nima.2021.165733>
20. N. Cruz, B. Santos, A. Fernandes et al., The design and performance of the real-time software architecture for the ITER radial neutron camera. *IEEE Trans. Nucl. Sci.* **66**(7), 1310–1317 (2019). <https://doi.org/10.1109/TNS.2019.2907056>
21. A. Fernandes, N. Cruz, B. Santos et al., FPGA code for the data acquisition and real-time processing prototype of the ITER radial neutron camera. *IEEE Trans. Nucl. Sci.* **66**(7), 1318–1323 (2019). <https://doi.org/10.1109/TNS.2019.2903646>
22. V.T. Jordanov, Pile up real time pulse shape discrimination based on ballistic deficit measurement and digital time invariant pulse shaping. In: 2018 IEEE nuclear science symposium and medical imaging conference (NSS/MIC), Sydney, Australia 10–17 Nov (2018). <https://doi.org/10.1109/NSSMIC.2018.8824502>
23. M. Nakhostin, Digital discrimination of neutrons and γ -rays in liquid scintillation detectors by using low sampling frequency ADCs. *Nucl. Instrum. Methods A* **916**, 66–70 (2019). <https://doi.org/10.1016/j.nima.2018.11.021>
24. J. Zhang, M.E. Moore, Z. Wang et al., Study of sampling rate influence on neutron-gamma discrimination with stilbene coupled to a silicon photomultiplier. *Appl. Radiat. Isot.* **128**, 120–124 (2017). <https://doi.org/10.1016/j.apradiso.2017.06.036>
25. S. Yang, X.Q. Zhang, C.M. Deng et al., Design of portable multifunction radiation detection system. *Nuclear Techniques* **45**(11), 110403 (2022). <https://doi.org/10.11889/j.0253-3219.2022.hjs.45.110403>. (in Chinese)
26. H.Q. Zhang, M.M. Yan, J.Y. Liu, Digitalization of filter shaping circuit for nuclear pulse signal. *Nuclear Techniques* **42**(7), 070402 (2019). <https://doi.org/10.11889/j.0253-3219.2019.hjs.42.070402>. (in Chinese)
27. Z.D. Li, H.Q. Zhang, J.Y. Liu et al., Implementation and analysis of Gaussian shaping method for digital nuclear pulse signal. *Nuclear Techniques* **42**(6), 060403 (2019). <https://doi.org/10.11889/j.0253-3219.2019.hjs.42.060403>. (in Chinese)
28. Q. Ge, L. Ge, H. Yuan et al., A new digital Gaussian pulse shaping algorithm based on bilinear transformation. *Nucl. Sci. Tech.* **26**, 010402 (2015). <https://doi.org/10.13538/j.1001-8042/nst.26.010402>
29. W. Chen, J.B. Zhou, F. Fang et al., Design of digital multi-channel spectrometer based on auto-baseline restoration. *Nuclear Techniques* **41**(5), 050401 (2018). <https://doi.org/10.11889/j.0253-3219.2018.hjs.41.050401>. (in Chinese)
30. W. Xiao, A.T. Farsoni, H. Yang et al., A new pulse model for NaI(Tl) detection systems. *Nucl. Instrum. Methods A* **763**, 170–173 (2014). <https://doi.org/10.1016/j.nima.2014.06.022>
31. Y. Liu, M. Wang, W. Wan et al., Counting-loss correction method based on dual-exponential impulse shaping. *J. Synchrotron Radiat.* **27**, 1609–1613 (2020). <https://doi.org/10.1107/S1600577520010954>
32. J. Lanchares, O. Garnica, J.L. Risco-Martín et al., Real-time evolvable pulse shaper for radiation measurements. *Nucl. Instrum. Methods A* **727**, 73–83 (2013). <https://doi.org/10.1016/j.nima.2013.05.164>
33. J. Liu, J. Yang, G. Zeng et al., Implementation of a cusp-like for real-time digital pulse shaper in nuclear spectrometry. *Nucl. Sci. Tech.* **28**, 103 (2017). <https://doi.org/10.1007/s41365-017-0248-1>
34. V.T. Jordanov, G.F. Knoll, Digital synthesis of pulse shapes in real time for high resolution radiation spectroscopy. *Nucl. Instrum. Methods A* **345**, 337–345 (1994). [https://doi.org/10.1016/0168-9002\(94\)91011-1](https://doi.org/10.1016/0168-9002(94)91011-1)
35. S. Saxena, A.I. Hawari, Digital pulse deconvolution with adaptive shaping for real-time high-resolution high-throughput gamma spectroscopy. *Nucl. Instrum. Methods A* **954**, 161288 (2020). <https://doi.org/10.1016/j.nima.2018.09.123>
36. X. Wang, J. Zhou, M. Wang et al., Signal modeling and impulse response shaping for semiconductor detectors. *Nucl. Sci. Tech.* **33**, 46 (2021). <https://doi.org/10.1007/s41365-022-01027-9>
37. D. Ponomarev, D. Filosofov, J. Khushvaktov et al., NaI(Tl+Li) scintillator as multirange energies neutron detector. *JINST* **16**, P12011 (2021). <https://doi.org/10.1088/1748-0221/16/12/P12011>
38. G. Rusev, M. Jandel, M. Kr̆ĭčka et al., Cascade γ rays following capture of thermal neutrons on ^{113}Cd . *Phys. Rev. C* **88**, 057602 (2013). <https://doi.org/10.1103/PhysRevC.88.057602>
39. J. Scherzinger, J.R.M. Annand, G. Davatz et al., Tagging fast neutrons from an $^{241}\text{Am}/^9\text{Be}$ source. *Appl. Radiat. Isot.* **98**, 74–79 (2015). <https://doi.org/10.1016/j.apradiso.2015.01.003>
40. S. Croft, The use of neutron intensity calibrated $^9\text{Be}(\alpha, n)$ sources as 4438 keV gamma-ray references standards. *Nucl. Instrum. Methods Phys. Res. A* **281**, 103–116 (1989). [https://doi.org/10.1016/0168-9002\(89\)91221-7](https://doi.org/10.1016/0168-9002(89)91221-7)

Springer Nature or its licensor (e.g. a society or other partner) holds exclusive rights to this article under a publishing agreement with the author(s) or other rightsholder(s); author self-archiving of the accepted manuscript version of this article is solely governed by the terms of such publishing agreement and applicable law.